Materials Science & Engineering A 802 (2021) 140655

Contents lists available at ScienceDirect

Materials Science & Engineering A

journal homepage: http://www.elsevier.com/locate/msea

A novel die-casting Mg alloy with superior performance: Study of microstructure and mechanical behavior

Yang Bai [a], Bing Ye [a,*], Liyang Wang [a], Beibei Zhao [a], Xin Yu [a], Yong Lu [c], Xiangyang Kong [b], Wenjiang Ding [a]

[a] National Engineering Research Center of Light Alloy Net Forming and State Key Laboratory of Metal Matrix Composites, Shanghai, 200240, China
[b] Institute of Materials for Mobile Energy, School of Materials Science and Engineering, Shanghai Jiao Tong University, Shanghai, 200240, China
[c] Shandong Yabaite Technology Co. Ltd, Shandong, 277116, China

ARTICLE INFO

Keywords:
Mg–Y–Zn alloys
High pressure die-casing
Mechanical properties
Grain refinement
Strengthening effect

ABSTRACT

In this work, a novel Mg–6Y–3Zn–1Al (WZA631, wt.%) alloy with great performance is successfully prepared through high pressure die-casting method, and microstructure characteristics and mechanical behavior are systematically investigated. Results show that the WZA631 alloy is primarily composed of equiaxed α-Mg grain, block and irregular $(Al,Zn)_2Y$ phases, as well as honeycomb-shaped 18R long period stacking ordered (LPSO) phase. The α-Mg grain has finer average grain size than other die-casting Mg alloys and $(Al,Zn)_2Y$ phase with cubic structure (a = 0.76 nm) is firstly reported. Mechanical tests demonstrate that yield strength, ultimate tensile strength, and elongation of the studied alloy at room temperature are 175 MPa, 281 MPa and 9.8%, respectively, which is better compared with existing commercial or some newly die-casting alloys. For the yield strength, grain boundary strengthening, solid solution strengthening and second phase strengthening are dominant contribution mechanisms. Superior ultimate tensile strength and elongation is attributed to the abnormal work-hardening effect in stage III due to joint action of solute atoms (Y and Zn) as well as coherent LPSO phases. Underlying principles of grain refinement, strengthening effect and work-hardening are well discussed.

1. Introduction

Magnesium (Mg) and its alloys, due to low density and high specific strength, are receiving increasing attention in automotive, aerospace and electronics fields [1–5]. The high pressure die-casting (HPDC) is a popular production method among various methods of fabricating Mg alloy parts, has clear merits such as better dimensional accuracy, higher production rate, and greater economic benefit [2,6–9]. Currently, the mainstream commercial HPDC Mg alloys are Mg–Al–Zn (AZ), Mg–Al–Mn (AM) and Mg–Al-RE (AE) series alloys [10–14], while their poor creep behavior and/or inadequate tensile properties (strength and elongation) hamper the widening application. Therefore, a series of works are conducted to improve performance of HPDC Mg alloys by altering process parameters or adding favorable elements [2,15–18]. For example, based on experimental results and theoretical analysis, Li et al. found that the strength and ductility of HPDC AZ91D alloy are concurrently raised through invoking turbulent melt flow into gating system [2], in which aroused shear stress obviously decreased the content of externally solidified crystals and porosity. Terada et al. reported by adding Ca elements to HPDC AM50 alloy, the alloy exhibited attractive creep resistance resulting from the preferential formation of thermally stable Al_2Ca phase replacing $Mg_{17}Al_{12}$ phase [15,16]. Lv et al. revealed that Gd element contributed to grain refinement and the formation of different intermetallic phase in AE43 alloy, leading to a significant improvement in tensile properties [19].Yang et al. demonstrated that trace Sr, B, Ca and Sm addition enhanced mechanical properties of HPDC AE series alloys at room and elevated temperature [13,17,18,20]. Furthermore, some efforts have been tried to improve mechanical properties of HPDC Mg alloys through vacuum process and heat treatment [6,10]. However, the aforementioned methods are relatively complicated and/or limited in terms of improving alloy properties, tensile properties in particular. In addition, researchers also developed new die-casting Mg alloys such as Mg–Sn–Ce and Mg–Al–Sn alloys [7,21], but their strength was low compared with some existing commercial alloys. Thus, it is required to exploit a new HPDC Mg alloy offering great performance.

* Corresponding author.
E-mail addresses: bingye@sjtu.edu.cn (B. Ye), xykong@sjtu.edu.cn (X. Kong).

https://doi.org/10.1016/j.msea.2020.140655
Received 28 October 2020; Received in revised form 5 December 2020; Accepted 7 December 2020
Available online 11 December 2020

In recent years, Mg–Y–Zn alloys with long period stacking ordered (LPSO) structure have attracted enormous interest attributing to their exceptional behavior in microstructure and properties aspects [4, 22–24]. In 2001, Kawamura et al. prepared a high-performance Mg–Y–Zn alloy with a yield strength of 610 MPa and an elongation of 5% using rapidly solidified powder metallurgy method [25]. The ultrahigh strength came from both fine grain strengthening and LPSO strengthening [26].Subsequently, based on this strengthening method, numerous researchers also have successfully developed high strength Mg–Y–Zn alloys through extrusion, rolling, forging and other thermal-mechanical processing methods [22,23,27]. Namely, it may be expected to develop great performance die-casting Mg alloys utilizing LPSO strengthening effect and microstructure refinement by HPDC. Even though there are an HPDC Mg–Zn–La–Y alloy in current literature, only compression properties and trace amounts of LPSO are found in the studied alloy [28]. Therefore, the detailed data is still scarce about the microstructure characteristics and tensile behavior of LPSO-based HPDC Mg alloys.

Previous works indicated that Y/Zn mole ratio is an key factor controlling phase composition of Mg–Y–Zn alloys, and the alloy is composed of α-Mg and LPSO when Y/Zn mole ratio is over 1.32 [24,29]. Aluminum is added to improve casting capability and refine grain [10,30,31]. In this work, a Mg–6Y–3Zn–1Al (WZA631, wt. %) alloy with LPSO phase (1.47 mol ratio) is designed and prepared via high pressure die-casting method. Then, the microstructure characteristics and tensile behavior are systematically characterized, and corresponding grain refinement and strengthening mechanisms are analyzed in detail. This can provide new data for the knowledge base of die-casing Mg alloys.

2. Experimental methods

Mg–6Y–3Zn–1Al (WZA631, wt.%) alloys were prepared from pure Mg (99.9%), pure Zn (99.9%), pure Al (99.9%) and Mg-30 wt% Y master alloy. At first, pure Mg were melted in a resistance furnace at 760 °C with mixture of continuous CO_2 and SF_6 gases for protection. Subsequently, the furnace temperature was adjusted to 740 °C and stirred for 5 min to ensure uniform distribution of alloying elements in melt. Finally, as the temperature naturally cooled to 720 °C, the melt was poured into a 400-ton cold chamber die-casting machine (DCC-400, China) to yield four rectangular plates with dimensions of 100 × 20 × 2.5 mm. And, prior to die-casting, the temperature of cold mold was raised to 200 °C by heating function in machine. The actual chemical composition of the obtained alloy was examined by inductively coupled plasma optical spectrometry (ICP-6300), as exhibited in Table 1.

Phase types of WZA631 alloy were detected using X-ray diffractometry (XRD, Ultima IV) with a step rate of 2°/min at angle range between 20°~80°. The melting temperatures of α-Mg and second phases were determined via differential scanning calorimetry (DSC, STA449F3) equipment at Ar atmosphere and heating speed of 2 °C/min. Microstructure characteristics were observed through a scanning electron microscope (SEM, Mira 3) and two transmission electron microscopes (TEM, JEM-2100F and FEI Tecnai G2 F20). Microscope instruments have energy-dispersive spectrometer (EDS). The average grain size was measured by selecting at least three microstructure images based on Nano Measurer 1.2 software. The tensile samples were processed at wire cutting machine, and its corresponding size were 12 mm in gauge length, 3.5 mm in width and 2.5 mm in thickness. Skin layer about 0.3 mm from each side of the surface were removed by polishing for tensile samples, and microstructure characterizations were conducted on the tensile sample surface. Tensile experiments were performed at crosshead speed of 0.2 mm/min by an electronic universal testing machine (WDW-10s) at room temperature. Samples was tested 5 times to ensure accuracy of data.

Table 1
Actual chemical composition of the obtained alloy.

Alloy	Nominal composition	Actual composition (wt%)			
		Y	Zn	Al	Mg
WZA631	Mg–6Y–3Zn–1Al	6.35	3.00	0.73	Bal.

3. Results

3.1. Microstructure characterization

Fig. 1 gives microstructure and grain size distribution of WZA631 alloy. As shown in Fig. 1a and b, the alloy microstructure mainly contains α-Mg equiaxed grains and intermetallic compounds locating at grain interior or grain boundary. Based on grain size distribution in Fig. 1c, the average grain size (AGS) is determined as 5.3 ± 0.5 μm that is finer compared with traditional die-casting Mg–Al series alloys [13]. At the same time, it can be observed in Fig. 1b the studied alloy has two different contrast intermetallic compounds divided into bright and gray phases. Bright phases display two morphologies including block shape (point A) and irregular shape (points B and C). Gray phases present a honeycomb-shaped, resembling to that of LPSO in Mg-RE-Zn alloys, at grain boundaries (point D) [32]. EDS mappings (Fig. 1d–f) show that Y, Zn and Al elements are enriched in bright phases (points A-C), while gray phases (point D) only demonstrate segregation of Y and Zn elements. Furthermore, the point analysis of bright and gray phases is summarized in Table 2. The bright phases (points A-C) exhibit a (Al, Zn)/Y ratio of nearly 2:1, similar to atoms ratio of Al_2Y [5]. However, since the phase composition and detailed crystal structure information for Al–Zn–Y phase are not available in the references, they are temporarily referred to as unknown phase. The gray phase (point D) with the composition of $Mg_{92.93}Y_{3.08}Zn_{3.99}$ is LPSO and analogous information is found in the work by Ye et al. [1].

Fig. 2 gives XRD pattern of WZA631 alloy. Phase types of the alloy are composed of α-Mg, LPSO and unknown phase. Based on Jade 5.0 software analysis, the diffraction peaks of unknown phase at 32.1°, 37.8°, 39.8° and 57.3° are close to those of Al_2Y crystal structure. And, combining with a (Al, Zn)/Y ratio of nearly 2:1of unknown phase in EDS results (Table 2), thus the phase is inferred as $(Al,Zn)_2Y$ phase having Al_2Y structure. This is further analyzed by TEM examination. Also, there are two small peaks about W phase ($Mg_3Zn_3Y_2$) in XRD pattern, but the phase cannot be found in SEM image and following DSC curve of this work owing to its low content.

Fig. 3 gives TEM images of block phase in Fig. 1b. From Fig. 3a and b, EDS mappings of the block phase illustrate uniform distribution of Al, Y, and Zn elements except Mg one, and the corresponding EDS point analysis in Fig. 3c shows atomic ratio of (Al, Zn): Y is about 2:1, which is consistent with SEM EDS results in Fig. 1. Fig. 3d–e presents selected area electron diffraction (SAED) of block phase along [001] and [$1\bar{1}2$] beam directions. The SAED shows a typical cubic diffraction pattern similar to Al_2Y structure and is very different from C36 structure in $(Al, Mg)_2X$ compounds [5,13]. Based on high-resolution TEM (HRTEM) image of Fig. 3f, the measured lattice parameter of block phase is 0.76 nm and close to that of Al_2Y (a = 0.79 nm). The above information strongly suggests the block phase is $(Al,Zn)_2Y$ compound. The difference of lattice parameters is attributed to substitution of Zn atoms for parts of Al atoms (r_{Zn} = 0.13 nm, r_{Al} = 0.14 nm). Note that, some Mg atoms may come from the Mg matrix background observed in EDS point analysis of Fig. 3c and these phenomenon are also found other Al_2RE phase such as Al_2Gd and Al_2Y etc [5,19].

Fig. 4a–c shows TEM image of irregular phase in Fig. 1b and its SAED patterns along [001] and [110] directions. As can be found, the intermetallic compound has the diffraction spots similar to above block $(Al, Zn)_2Y$ phase, implying that irregular phase has $(Al,Zn)_2Y$ crystal structure. Based on point and mapping data of EDS in Fig. 4d–h, the phase is also enriched by Y, Zn and Al elements, and has near 2 of (Al, Zn)/Y

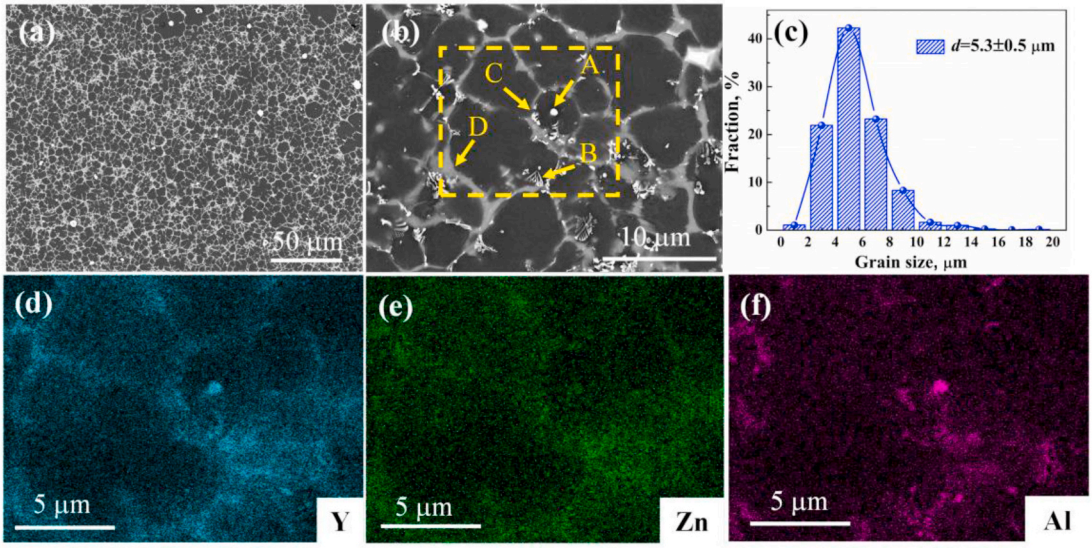

Fig. 1. Microstructure characteristics of WZA631 alloy: (a, b) SEM images, (c) grain size distribution, (d–f) EDS mappings corresponding to yellow box area in Fig. 1b. (For interpretation of the references to colour in this figure legend, the reader is referred to the Web version of this article.)

Table 2
EDS results in Fig. 1b.

Position	Mg (at. %)	Y (at. %)	Zn (at. %)	Al (at. %)	Phase
A	10.68	31.41	2.99	53.92	Unknown
B	85.04	4.99	3.27	6.70	
C	88.05	6.28	4.69	7.26	
D	92.93	3.08	3.99	–	LPSO

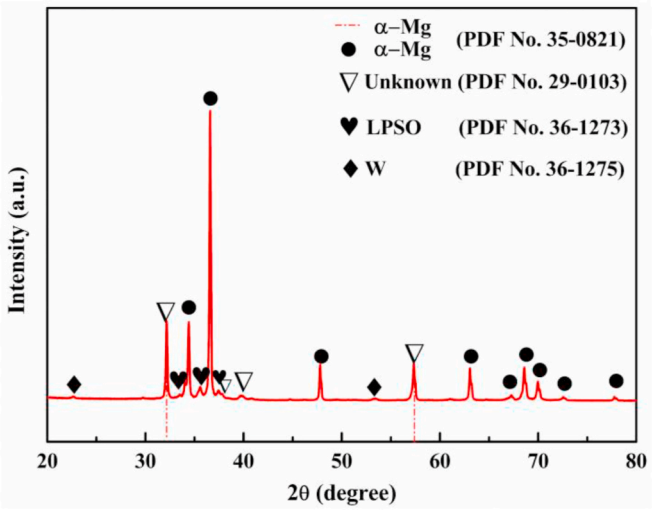

Fig. 2. XRD pattern of WZA631 alloy.

elements ratio. In addition, numerous Mg elements are almost uniformly distributed except at several spots with much enriched Al, Zn and Y elements from EDS data, which means the phase contains part of α-Mg matrix. Thus, the irregular phase should be an eutectic phase consists of α-Mg and $(Al,Zn)_2Y$ phase.

Fig. 5 gives TEM and HRTEM images of LPSO phase in Fig. 1b as well as its SAED patterns with electron beam along $[11\bar{2}0]$of Mg matrix. In Fig. 5b, HRTEM image indicates that the measured lattice fringes spacing of LPSO is about 1.6 nm, approximately equaling to six times of $(0002)_{Mg}$ with 0.26 nm spacing, which is unique characters of 18R-LPSO structure [33]. Meanwhile, from (0000) to $(0002)_{Mg}$ spots of SAED in LPSO phase (Fig. 5c), there are six diffraction spots observed at positions n/6 (n represents integer), further suggests that the type of LPSO phase in this study as 18R. Besides, from the other two spots in Fig. 5c, $(100)_{18R}$ and $[1\bar{1}00]_{Mg}$, the 18R-LPSO has a coherent crystal relation with Mg matrix namely, $[010]_{18R}//[11\bar{2}0]_{Mg}$, *and* $(001)_{18R}//(0001)_{Mg}$ [4]. Fig. 5d shows that TEM EDS results of 18R-LPSO are nearly accordance with SEM EDS results in Table 2, having the composition of $Mg_{93.65}Y_{3.42}Zn_{2.93}$ [1].

Fig. 6 shows DSC curve of the WZA631 alloy, where each endothermic peak represents the melting point of an intermetallic compound. According to above SEM and TEM analysis, there are four types of intermetallic compounds in the studied alloy including α-Mg, block $(Al,Zn)_2Y$, irregular eutectic $(Al,Zn)_2Y$ and LPSO. This means that the DSC curve should have four endothermic peaks, however, only three peaks are observed in Fig. 6. The first endothermic peak at 629 °C is common melting point of α-Mg in Mg–Y–Zn alloys [24]. The third peak at 545 °C corresponds to decomposition or melting of LPSO consisting with previous research [22]. Due to eutectic phase usually has a low melting point relative to Mg matrix, the second peak at 607 °C between α-Mg and LPSO is speculated to be irregular eutectic $(Al,Zn)_2Y$ phase. Also, from literature reports, the endothermic peak of primary Al_2Y phase was about 692 °C [31], which is higher that of α-Mg and exceeds the detection range of instrument DSC in this work. Thus, this results in the primary block $(Al,Zn)_2Y$ phase similar to Al_2Y structure not being observed in DSC curve. In summary, melting points of second phases follow the order of block $(Al,Zn)_2Y$ > α-Mg > irregular eutectic $(Al,Zn)_2Y$ > LPSO.

3.2. Mechanical properties

Fig. 7a shows tensile curve and mechanical property values of WZA631 alloy. The yield strength (YS), ultimate tensile strength (UTS) and elongation (EL) of the alloy are 175 MPa, 281 MPa, 9.8%, respectively. Fig. 7b and c summarize YS, UTS and EL of various die-casting Mg alloys. The developed WZA631 alloy demonstrates a better balance feature of strength and plasticity compared to other commercial alloys such as AE44, AZ91, AM50A and AX51 [12,13]. Especially, as shown in Fig. 7c, the studied alloy exhibits the highest UTS in commercial and novel experimental die-casting Mg alloys except the ALaGd432 [7,8,10–13,17,21,28,34]. Strengthening effects related to superior properties in the alloy will be discussed in section 4.3.

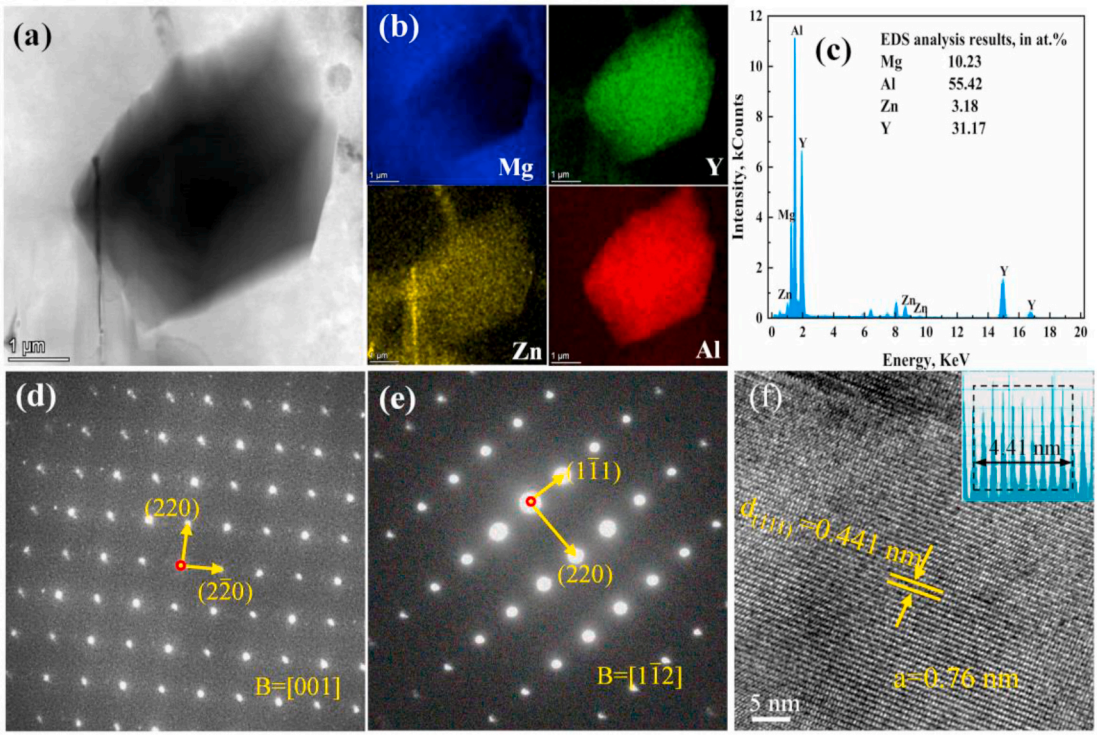

Fig. 3. TEM micrographs of block phase in Fig. 1b: (a) bright-field TEM image, (b–c) EDS mapping and point analysis, (d–e) SAED along [001] and [1$\bar{1}$2] directions, (f) High-resolution TEM image (inset: the distance between ten lattice fringes).

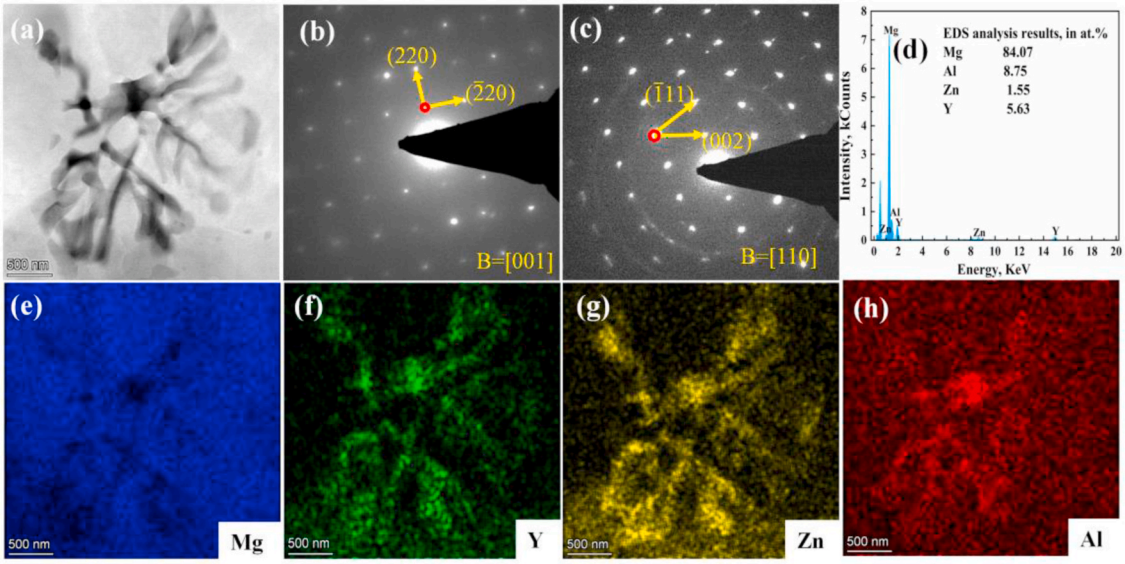

Fig. 4. TEM micrographs of irregular phase in Fig. 1b: (a) bright-field TEM image, (b–c) SAED along [001] and [110] beam directions and (d–h) EDS point and mapping analysis.

Fig. 8 shows SEM images of longitudinal and cross sections of WZA631 alloy after tensile fracture. As exhibited in Fig. 8a, fracture is primarily along second phases at grain boundaries indicated by yellow arrows. The $(Al,Zn)_2Y$ and LPSO second phases have high hard and brittle characteristics compared with Mg matrix, resulting in stress concentration and acting as formation points of micro-cracks during deformation. Furthermore, it can be found from Fig. 8b that fracture morphology of the alloy consists of cleavage steps, tear ridges and small dimples. Namely, the failure mode in the alloy is a mixture combination of brittle and ductile fracture. The cleavage steps usually represent occurrence of intergranular fracture mode (brittle fracture) resulting from propagation of cracks along intermetallic compounds at grain boundaries. However, small dimples develop from cracks at grain interior induced by stress transferring at grain boundaries, which means transgranular fracture (ductile fracture).

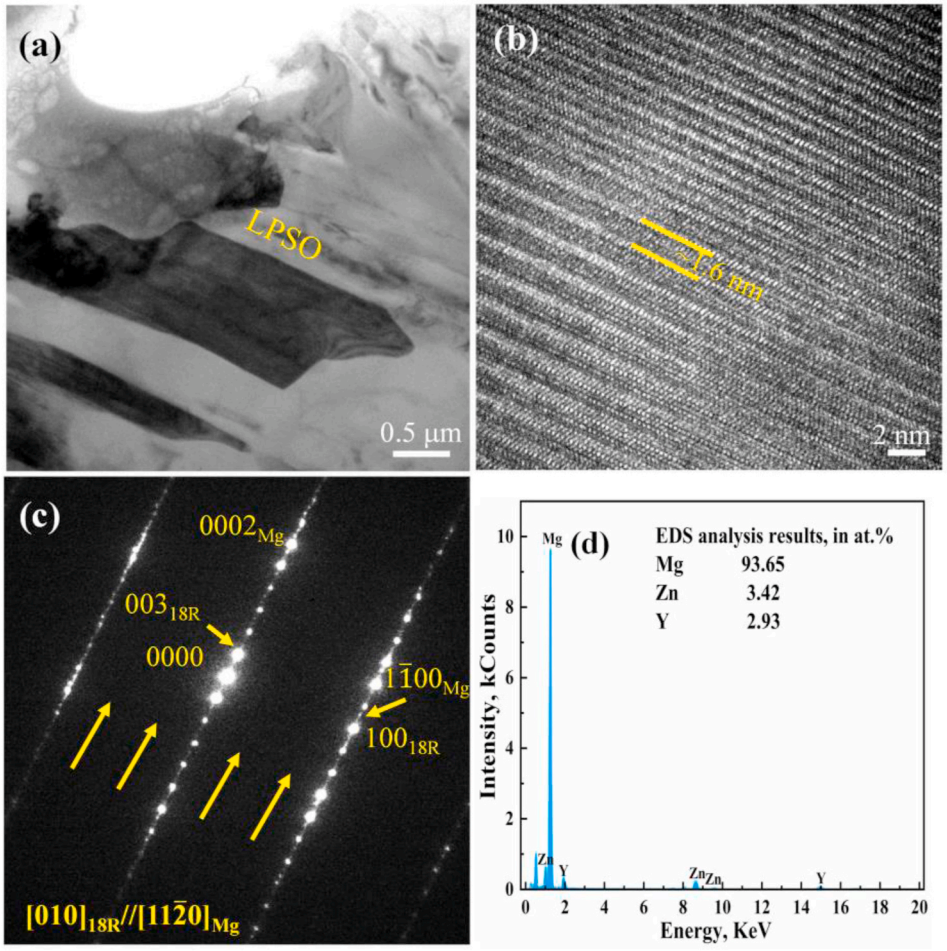

Fig. 5. TEM micrographs of LPSO phase in Fig. 1b: (a) bright-field TEM image, (b) High-resolution TEM image, (c) SAED along [11$\bar{2}$0]beam direction and (d) EDS point analysis.

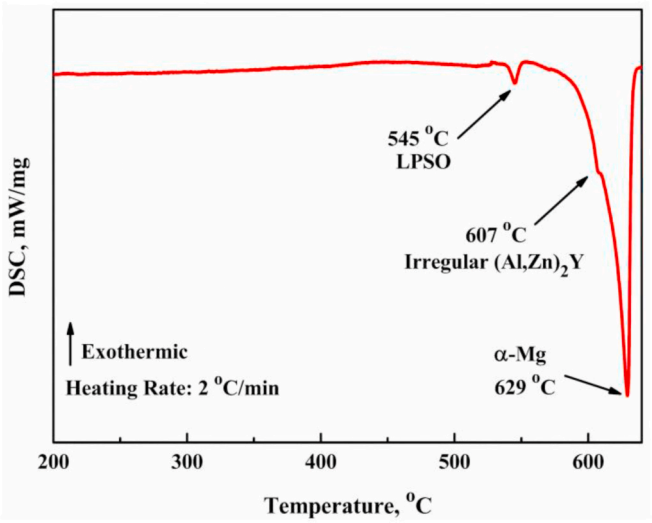

Fig. 6. Differential scanning calorimetry (DSC) curve of WZA631 alloy.

4. Discussion

4.1. Grain refinement

From Fig. 1c, the present WZA631 alloy shows an average grain size (AGS) of about 5.3 μm. The AGS of the alloy is relatively fine compared with new die-casting alloys including ALaGd432, AGd44, AEX422 and ZLaW423 (6.1 μm, 5.9 μm, 7 μm, 6.1 μm) [13,19,28,35]. Moreover, the AGS is smaller with respect to commercial die-casting alloys, AZ91, AM60B, AE44, AS21 and AX53 alloys, with reduction of 30%, 34%, 62%, 44% and 47% (7.6 μm, 8 μm, 14 μm, 9.5 μm, 10 μm), respectively [6,13,36–38]. This fine grain size is mostly correlated with solute atoms and second phases of alloys.

During solidification, the solute elements are redistributed and enrich in front of solid-liquid interface, inducing formation of constitutional undercooling, which will stimulate grains continue nucleation and thus obstruct grains growth [39,40]. The effect of constitutional undercooling for solutes can be expressed using growth restriction factor Q,

$$Q = \left(\frac{\partial(\Delta T_{cs})}{\Delta f_s}\right)_{\Delta fs \to 0} \quad (1)$$

where $\Delta Tcs = T_L\text{-}T$ is constitutional undercooling (T_L and T are liquidus temperature and actual temperature), f_s is solid fraction. The functional correlation between ΔTcs and fs is described through Schell model of Pandat software for various die-casting Mg alloys, as exhibited in Fig. 9a. The more specific methods are acquired in the research by Schmid-Fetzer et al. [41]. Then, combing with equation (1) and Fig. 9a, Q values of WZA631 and other die-casting Mg alloys are determined and shown in Fig. 9b. As indicated, the Q value of WZA631 alloy is relatively high among these alloys, implying constitutional undercooling (solutes) plays an important function in grain refinement. Moreover, numerous

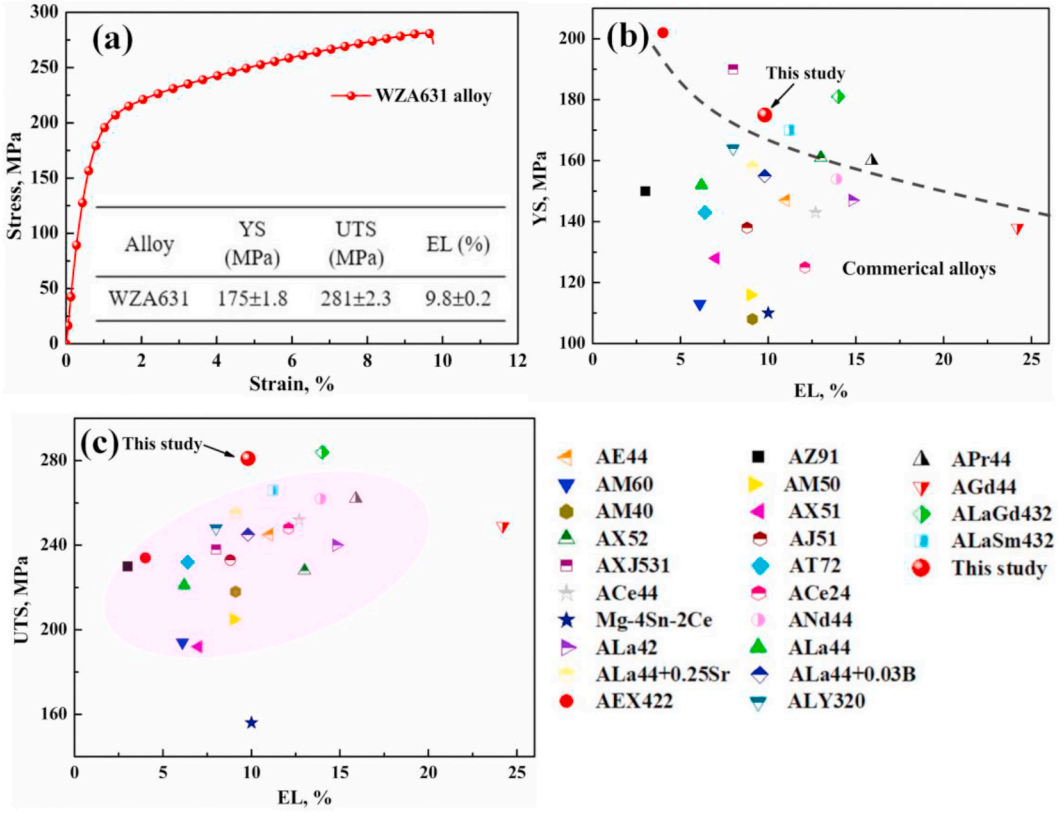

Fig. 7. (a) Tensile curve and corresponding mechanical property values of WZA631 alloy; (b, c) YS, UTS and EL of various die-casting Mg alloys [7,8,10–13,17,21,28,34].

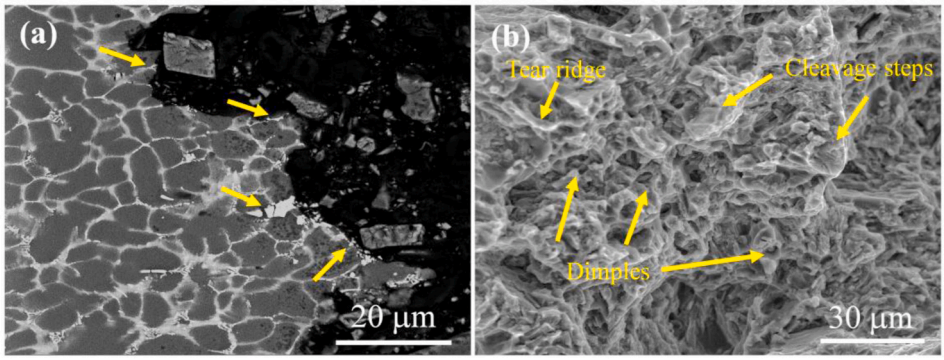

Fig. 8. SEM images of WZA631 alloy after tensile fracture: (a) longitudinal section and (b) cross section.

fine gray LPSO in Fig. 1b phases distribute along grain boundaries which also contribute to decreasing grain size. LPSO phases having good thermal stability, high hardness and elastic modulus, may serve as pinning sites for grain growth during solidification [24,32]. Similar phenomenon is reported by other researchers who demonstrated fine LPSO phase caused grain refinement through blocking boundaries migration [23,42]. In addition, SEM image in Fig .1a shows the block bright $(Al,Zn)_2Y$ phases exists in α-Mg grain interior, implying that parts of block phases may be heterogeneous nucleation sites of α-Mg. Other Al_2RE particles locating inside grain, such as Al_2Y, Al_2Gd, Al_2Sm and Al_2Nd, have also been reported as nucleation substrate and refine grain size of Mg matrix [43]. In summary, the fine grain size of WZA631 alloy is primarily ascribed to synergistic refinement effect of solute atoms for constitutional supercooling, LPSO phases for grain restricting and block $(Al,Zn)_2Y$ phases for heterogeneous nucleation.

4.2. *Solidification analysis*

In this work, the grain structure of WZA631 alloy shows a typical equiaxed morphology that differs from dendritic structure common in Mg–Y–Zn series alloys. This is attributed to high cooling rate and high liquid flow velocity during die-casting process. The high cooling speed is anticipated to cause large concentration gradient and this conversely raises the liquidus gradient, resulting in a high constitutional undercooling. According to grain nucleation equation [44], the larger constitutional undercooling usually means smaller grain nucleation radius and nucleation work, which in turn leads to grain refinement and formation of equiaxed grains at solid-liquid interface. Also, the high liquid flow velocity induces dendritic fragmentation and superheat loss of the melt that contributes to enhancing the nucleation chance of equiaxed grains at interface.

For further understanding microstructure evolution of the alloy, the

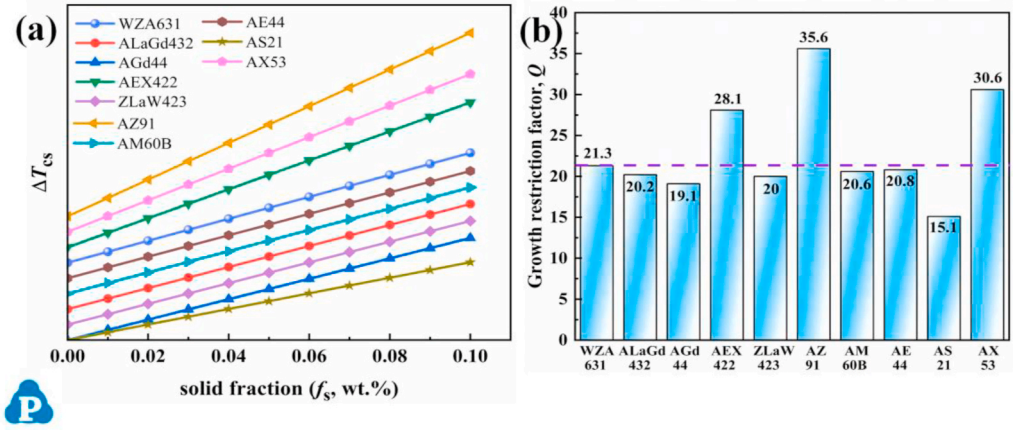

Fig. 9. (a) The linear relationship between constitutional undercooling (ΔT_{cs}) and solid fraction (f_s) obtained from Schell model of Pandat software, and (b) the calculated restrictor factor (Q) for various die-casting Mg alloys.

solidification models are provided in Fig. 10. Table 3 gives mixing enthalpy and electronegativity discrepancy of alloy solutes in the melt condition [45]. As can be found, the mixing enthalpy and electronegativity discrepancy of Al and Y (−38, 0.39) atoms are higher than other element combinations, implying Al–Y compounds is easily formed during solidification. Moreover, the difference of these thermodynamic parameters between Al and Zn are very small that suggests Zn atoms may replace parts of Al atoms during the formation of Al–Y compound, consequently, leading to the formation of $(Al,Zn)_2Y$ phase confirmed in above TEM results. Meanwhile, combined with DSC curve analysis of Fig. 6, primary $(Al,Zn)_2Y$ phase has the highest melt point among other phases. Thus, $(Al,Zn)_2Y$ phase first is generated during solidification and may act as nucleation sites for α-Mg through reaction L+$(Al,Zn)_2Y$→α-Mg (Fig. 10a–b) [31]. As solidification progress, some α-Mg grains spontaneously nucleate at 629 °C by formula L→α-Mg (Fig. 10c). Simultaneously, the solubility of solute elements in magnesium gradually decrease as temperature decreasing, in which Y, Zn and Al atoms escape from melt and enrich at front of solid-liquid interface (Fig. 10c). After that, theses solute atoms at interface will react and form intermetallic compounds along grain boundaries by eutectic or peritectic reaction. When the temperature falls to 607 °C, the irregular $(Al,Zn)_2Y$ phase is obtained through eutectic equation L →α-Mg+ $(Al,Zn)_2Y$ (Fig. 10d). Finally, the remaining Y and Zn atoms in liquid interact with α-Mg to generate LPSO at 545 °C based on transformation L+α-Mg→LPSO [46]. The formed LPSO surrounds α-Mg and causes grain refinement through restricting boundaries migration (Fig. 10e).

Table 3
Mixing enthalpy and electronegativity discrepancy of alloy elements in the melt condition.

Properties	Elements combination					
	Mg–Y	Mg–Zn	Mg–Al	Al–Y	Zn–Y	Al–Zn
Mixing enthalpy, kJ/mol	−6	−4	−2	−38	−31	1
Electronegativity discrepancy	0.09	0.34	0.30	0.39	0.43	0.04

4.3. Strengthening effect

From Fig. 7, the WZA631 alloy shows a great balance for strength and ductility compared to other HPDC Mg alloys. Such performance is strongly related to grain size, solute atoms and second phases. Firstly, the finer grain size of WZA631 alloy means more grain boundaries existing in the Mg matrix, that is more obstacles and higher energy to dislocation slip, and thereby resulting in higher strength [13]. The strengthening effect (σ_{gs}) of grain size on yield strength is estimated through typical Hall-Petch equation,

$$\sigma_{gs} = \sigma_0 + kd^{-1/2} \quad (2)$$

where, σ_0 is the friction stress in MPa, k is the Hall-Petch slope and d is the AGS ~5.3 μm. To clearly estimate reinforcement contribution of grain size, the used σ_0 and k are acquired based on pure magnesium,

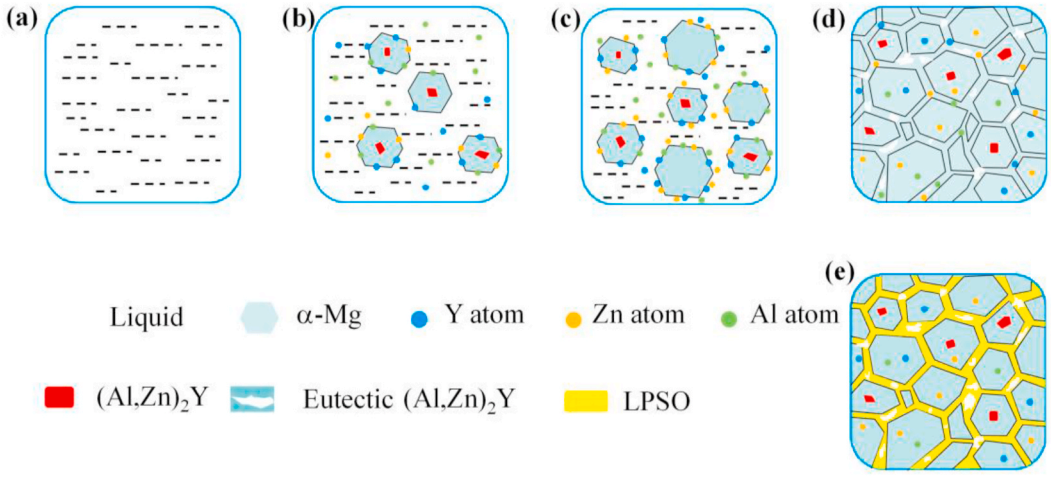

Fig. 10. Schematic diagram of microstructure evolution for WZA631 alloy during solidification process.

which are 11 MPa and 220 MPa $\mu m^{1/2}$, respectively [47]. The σ_{gs} is calculated as 107 MPa.

Secondly, Y, Zn and Al atoms have high solid solubility in Mg matrix owing to high cooling rate for die-casing process. Moreover, there are big crystal lattice strain for Mg matrix due to the difference in size between Mg atoms and solutes, making dislocation movement difficult [48]. As a result, yield strength of WZA631 alloy is enhanced by solute atoms. The solid solutes strengthening effect (σ_{ss}) is determined as [49],

$$\sigma_{ss} = M(38.9)\left\{\left(\frac{\varepsilon_b}{0.176}\right)^2 + \left(\frac{\varepsilon_{SFE}}{5.67}\right)^2 - \frac{\varepsilon_b \varepsilon_{SFE}}{2.98}\right\}^{3/2} \Delta c_s^{1/2} \quad (3)$$

where, M is Taylor factor equaling to 4.5, ε_b is size discrepancy (%), ε_{SFE} is chemical discrepancy and c_s is atomic concentration (at. %). From simulation results in Ref. [49], the values of ε_b and ε_{SFE} pair are considered as 21.2 and −1.7 for Y atom, −15.3 and 0.32 for Zn atom, −11.5 and −1.25 for Al atom, respectively. According to energy dispersive spectrometer examination in TEM instrument, concentration c_s of Y, Zn and Al atoms is 1.01, 0.90 and 0.08, and thus the total σ_{ss} is calculated as 50 MPa.

Thirdly, strengthening effect (σ_{ps}) of second phases to yield strength mainly links to LPSO phase due to its unique characteristics and much higher volume fraction than that of $(Al,Zn)_2Y$ phase. Strengthening effects of LPSO are divided into following three aspects: LPSO phase owns higher modulus and hardness relative to Mg matrix, which can endure stress transferring deriving from matrix during deformation through shear-lag principle, and thus occur load transfer strengthening [32,33,50]; LPSO phase may serve as obstruction for grain boundaries sliding and enhance the activation stress of basal dislocations [51]; the kinking bands of LPSO caused by deformation refine grain and offer extra strengthening [32]. The strengthening contribution of LPSO phases is expressed by Orowan model (σ_{Or}) [52] and Load-transfer model (σ_{Lo}) [50,53].

$$\sigma_{ps} = \sigma_{Or} + \sigma_{Lo} \quad (4)$$

$$\sigma_{Or} = M\frac{0.4Gb}{\pi\sqrt{1-\nu}}\frac{\ln(2\bar{r}/b)}{\lambda} \quad (5)$$

$$\sigma_{Lo} = \sigma_m\left[\frac{V_p(s+2)}{2} + V_m\right] - \sigma_m \quad (6)$$

where G is shear modulus (16.6 GPa), b is the Burger vector (0.32 nm), ν is Poisson ratio (0.267), $\bar{r} = \sqrt{2/3}r$, $\lambda = 2\bar{r}(\sqrt{\pi/4V_p} - 1)$, r and V_p are mean radius and volume fraction of reinforcement phases, σ_m and V_m are yield stress and volume fraction of Mg matrix, s is the aspect ratio of LPSO phases. The values of r, s, Vp and V_m are determined to be 0.87 μm, 1.9, 20% and 76% through Image-Pro plus 6.0 software. Consequently, σ_{Or} and σ_{Lo} are estimated as 21.5 MPa and 23.5 MPa, and the total value of σ_{ps} is 45 MPa. Based on above strengthening analysis, it can be found that yield strength of WZA631 alloy benefits from grain boundary strengthening, solution strengthening and second phase strengthening. Table 4 lists the contribution values of various strengthening effect, and it suggests a few errors existing between computed and measured yield strength. This may be owing to bias of theoretical parameters utilizing in strengthening models and defects originating from die-casting procedure.

The very high UTS and moderate EL of WZA631 alloy depend on work-hardening behavior during plastic deformation. The behavior is usually evaluated by work-hardening rate (θ, $= d\sigma/d\varepsilon$) vs. flow stress increment (σ-$\sigma_{0.2}$) curve, where σ and ε represent true stress and true strain, respectively shown in Fig. 11a. Initially, as the (σ-$\sigma_{0.2}$) increases, the θ behaves a sharp decline phenomenon corresponding to elasto-plastic transition region (stage I). Subsequently, the θ gradually decreases and shows a linear relationship with (σ-$\sigma_{0.2}$), which is regarded as stage III of strain-hardening. Actually, the variation of hardening rate relies on interaction of dislocations accumulation and annihilation that can be expressed using θ (σ-$\sigma_{0.2}$) vs. (σ-$\sigma_{0.2}$) relation curve of Fig. 11b, where θ(σ-$\sigma_{0.2}$) and (σ-$\sigma_{0.2}$) mean dislocation storage and dislocation density, respectively [54]. As indicated, in the early stage, the curve exhibits a linear growth with slope θ_0 and θ_0 is associated with dynamic recovery in metal. Generally, high dynamic recovery rate (dislocations annihilation) represents small grain size and less precipitates in alloy [55]. As the value of (σ-$\sigma_{0.2}$) reaches 50 MPa, hardening region change elastoplastic region (stage I) in Fig. 11a to hardening stage III (Fig. 11b). However, after that, θ(σ-$\sigma_{0.2}$) of stage III gradually increases as the increment of (σ-$\sigma_{0.2}$), which is abnormal with falling curves reported in studies [54,55], implying that stage III of the studied alloy has higher dislocation storage and density (namely, strong work-hardening effect). The reasons are demonstrated from following points. From above solid solution strengthening section, the Al atoms concentration (0.08 at.%) is very low compared with Y and Zn atoms (1.01 at.% and 0.90 at.%), which indicates Y and Zn atoms have an essential role in strain hardening. The numerous Y and Zn solute atoms in the matrix inhibit subsequent dynamic recovery by pinning migrating dislocations, thus maintaining massive dislocations accumulation [56]. On the other hand, LPSO phase not only hinder dislocation movement and increase dislocation storage as hard $Mg_{17}Al_{12}$ and $Al_{11}RE_3$, but also its coherent interface with Mg matrix weakens occurrence of crack and twinning, promoting the improvement of ductility [32,51]. Additionally, it has been reported that fine grains promoted activation of multiple slip or enhanced dynamic recovery, which are adverse to dislocation storage in grain [55,57]. As mentioned above, solute atom and LPSO in this work facilitate accumulation and generation of dislocations during deformation process, enhancing work-hardening effect, resulting in both higher UTS and moderate EL.

Table 4
Contribution value of various strengthening mechanisms.

Strength mechanisms	Contribution value, MPa
Grain boundary strengthening, σ_{gs}	107
Solid solution strengthening, σ_{ss}	50
Second phase strengthening, σ_{ps}	45
Computed value, σ_y	202
Measured value, $\sigma_{0.2}$	175

5. Conclusion

In summary, a novel Mg–6Y–3Zn–1Al (WZA631, wt.%) alloy with superior performance has successfully been developed via high pressure die-casting method, and microstructure characteristics and mechanical behavior are well investigated. Key points are drawn as follows.

(1) The WZA631 alloy is primarily composed of equiaxed α-Mg grains, block $(Al,Zn)_2Y$ phase, irregular eutectic $(Al,Zn)_2Y$ phase and honeycomb-shaped 18R LPSO phase.
(2) The α-Mg grain has an average grain size of about 5.3 μm that is finer with respect other die-casting Mg alloys, and $(Al,Zn)_2Y$ phase with cubic structure (a = 0.76 nm) is firstly reported.
(3) The WZA631 alloy exhibits YS of 175 MPa, UTS of 281 MPa and EL of 9.8%, which has a great combination of strength and ductility compared with existing commercial and some newly die-casting Mg alloys.
(4) For YS, grain boundary strengthening, solid solution strengthening and second phase strengthening are predominant contribution mechanisms. The superior UTS and EL are attributed to the reinforced strain-hardening effect in stage III due to both solute atoms (Y and Zn) and coherent LPSO phases inhibiting dynamic recovery, maintaining dislocation storage as well as weaking occurrence of crack and twinning.

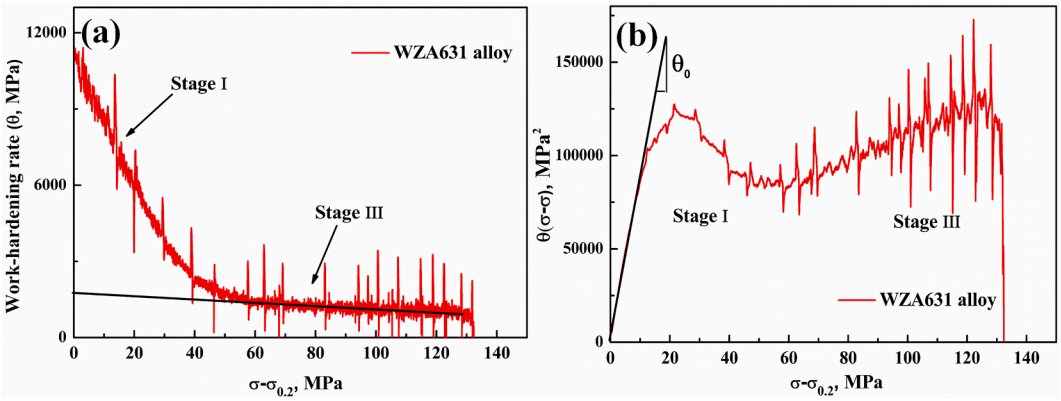

Fig. 11. Strain-hardening curve of WZA631 alloy: (a) work-hardening rate θ vs. flow stress increment (σ-$\sigma_{0.2}$) and (b) θ (σ-$\sigma_{0.2}$) vs. (σ-$\sigma_{0.2}$) curve.

Data availability

The raw/processed data required to reproduce these findings cannot be shared at this time as the data also forms part of an ongoing study.

CRediT authorship contribution statement

Yang Bai: Materials preparation, Data processing, Writing - original draft, Investigation. **Bing Ye:** Conceptualization, Supervision, Writing - review & editing. **Liyang Wang:** Materials preparation and Reviewing. **Beibei Zhao:** Reviewing. **Xin Yu:** Reviewing. **Yong Lu:** Reviewing. **Xiangyang Kong:** Supervision, Reviewing and Editing. **Wenjiang Ding:** Resources, Validation.

Declaration of competing interest

The authors declare that they have no known competing financial interests or personal relationships that could have appeared to influence the work reported in this paper.

Acknowledgements

This work was supported by the National Key Research and Development Program of China [grant number 2016YFB0700502, 2016YFB0301001]. The authors also acknowledge Dr. Chuan Zhang (CompuTherm LLC company, USA) for the help in using Pandat software.

References

[1] L. Ye, Y. Liu, D.S. Zhao, Y.L. Zhuang, S.B. Gao, X.Q. Liu, J.P. Zhou, J.N. Gui, J. B. Wang, Effects of Sn on the microstructure and mechanical properties of a hot-extruded Mg-Zn-Y-Sn alloy, Mater. Sci. Eng., A 724 (2018) 121–130.
[2] X. Li, W. Yu, J. Wang, S. Xiong, Influence of melt flow in the gating system on microstructure and mechanical properties of high pressure die casting AZ91D magnesium alloy, Mater. Sci. Eng., A 736 (2018) 219–227.
[3] K. Li, V.S.Y. Injeti, R.D.K. Misra, L.G. Meng, X.G. Zhang, The contribution of long-period stacking-ordered structure (LPSO) to high strength-high ductility combination and nanoscale deformation behavior of magnesium-rare earth alloy, Mater. Sci. Eng., A 713 (2018) 112–117.
[4] P. Cheng, Y. Zhao, R. Lu, H. Hou, Effect of the morphology of long-period stacking ordered phase on mechanical properties and corrosion behavior of cast Mg-Zn-Y-Ti alloy, J. Alloys Compd. 764 (2018) 226–238.
[5] G. Zhang, Y. Wang, Z. Liu, S. Liu, Influence of Al addition on solidification path and hot tearing susceptibility of Mg–2Zn–(3 + 0.5x)Y–xAl alloys, J. Magnes. Alloy. 7 (2019) 272–282.
[6] X.J. Wang, S.M. Zhu, M.A. Easton, M.A. Gibson, G. Savage, Heat treatment of vacuum high pressure die cast magnesium alloy AZ91, Int. J. Cast Metals Res. 27 (2013) 161–166.
[7] X. Shi, D. Li, A.A. Luo, B. Hu, L. Li, X. Zeng, W. Ding, Microstructure and mechanical properties of Mg-7Al-2Sn alloy processed by super vacuum die-casting, Metall. Mater. Trans. A 44 (2013) 4788–4799.
[8] C. Su, D. Li, J. Wang, R. Shi, A.A. Luo, X. Zeng, Z. Lin, J. Chen, Enhanced ductility in high-pressure die casting Mg-4Ce-xAl-0.5Mn alloys via modifying second phase, Mater. Sci. Eng., A 773 (2020).
[9] X. Dong, L. Feng, S. Wang, E.A. Nyberg, S. Ji, A new die-cast magnesium alloy for applications at higher elevated temperatures of 200–300 °C, J. Magnes. Alloy (2020), https://doi.org/10.1016/j.jma.2020.09.012.
[10] S.M. Zhu, T.B. Abbott, M.A. Gibson, J.F. Nie, M.A. Easton, Age hardening in die-cast Mg–Al–RE alloys due to minor Mn additions, Mater. Sci. Eng., A 656 (2016) 34–38.
[11] M. Su, J. Zhang, Y. Feng, Y. Bai, W. Wang, Z. Zhang, F. Jiang, Al-Nd intermetallic phase stability and its effects on mechanical properties and corrosion resistance of HPDC Mg-4Al-4Nd-0.2Mn alloy, J. Alloys Compd. 691 (2017) 634–643.
[12] A.A. Luo, Recent magnesium alloy development for elevated temperature applications, Int. Mater. Rev. 49 (2013) 13–30.
[13] Q. Yang, K. Guan, F. Bu, Y. Zhang, X. Qiu, T. Zheng, X. Liu, J. Meng, Microstructures and tensile properties of a high-strength die-cast Mg–4Al–2RE–2Ca–0.3Mn alloy, Mater. Char. 113 (2016) 180–188.
[14] Q. Xu, A. Ma, Y. Li, J. Sun, Y. Yuan, J. Jiang, C. Ni, Microstructure evolution of AZ91 alloy processed by a combination method of equal channel angular pressing and rolling, J. Magnes. Alloy. 8 (2020) 192–198.
[15] M.O. Pekguleryuz, A.A. Kaya, Creep resistant magnesium alloys for powertrain applications, Adv. Eng. Mater. 5 (2003) 866–878.
[16] Y. Terada, D. Itoh, T. Sato, Creep rupture properties of die-cast Mg–Al–Ca alloys, Mater. Chem. Phys. 113 (2009) 503–506.
[17] Q. Yang, T. Zheng, D. Zhang, X. Liu, J. Fan, X. Qiu, X. Niu, J. Meng, Microstructures and tensile properties of Mg–4Al–4La–0.4Mn–xB (x=0, 0.01, 0.02, 0.03) alloy, J. Alloys Compd. 572 (2013) 129–136.
[18] Q. Yang, F. Bu, T. Zheng, F. Meng, X. Liu, D. Zhang, X. Qiu, J. Meng, Influence of trace Sr additions on the microstructures and the mechanical properties of Mg–Al–La-based alloy, Mater. Sci. Eng., A 619 (2014) 256–264.
[19] S. Lv, X. Lü, F. Meng, Q. Yang, X. Qiu, P. Qin, Q. Duan, J. Meng, Microstructures and mechanical properties in a Gd-modified high-pressure die casting Mg–4Al–3La−0.3Mn alloy, Mater. Sci. Eng., A 773 (2020).
[20] Q. Yang, F. Bu, F. Meng, X. Qiu, D. Zhang, T. Zheng, X. Liu, J. Meng, The improved effects by the combinative addition of lanthanum and samarium on the microstructures and the tensile properties of high-pressure die-cast Mg–4Al-based alloy, Mater. Sci. Eng., A 628 (2015) 319–326.
[21] S. Ozarslan, H. Sevik, I. Sorar, Microstructure, mechanical and corrosion properties of novel Mg-Sn-Ce alloys produced by high pressure die casting, Mater. Sci. Eng. C 105 (2019) 110064.
[22] F. Qi, D. Zhang, X. Zhang, X. Xu, Effects of Mn addition and X-phase on the microstructure and mechanical properties of high-strength Mg–Zn–Y–Mn alloys, Mater. Sci. Eng., A 593 (2014) 70–78.
[23] K. Hagihara, A. Kinoshita, Y. Sugino, M. Yamasaki, Y. Kawamura, H.Y. Yasuda, Y. Umakoshi, Effect of long-period stacking ordered phase on mechanical properties of $Mg_{97}Zn_1Y_2$ extruded alloy, Acta Mater. 58 (2010) 6282–6293.
[24] Y. Bai, B. Ye, J. Guo, L. Wang, X. Kong, W. Ding, Mechanical properties and yield asymmetry of Mg-Y-Zn alloys: competitive behavior of second phases, Mater. Char. 164 (2020), 110301.
[25] Y. Kawamura, K. Hayashi, A. Inoue, Rapidly solidified powder metallurgy $Mg_{97}Zn_1Y_2$ Alloys with excellent tensile yield strength above 600 MPa, Mater. Trans. 42 (2001) 1172–1176.
[26] E. Abe, Y. Kawamura, K. Hayashi, A. Inoue, Long-period ordered structure in a high-strength nanocrystalline Mg-1at%Zn-2at%Y alloy studied by atomic-resolution -contrast STEM, Acta Mater. 50 (2002) 3845–3857.
[27] M. Yamasaki, K. Hashimoto, K. Hagihara, Y. Kawamura, Effect of multimodal microstructure evolution on mechanical properties of Mg–Zn–Y extruded alloy, Acta Mater. 59 (2011) 3646–3658.
[28] X. Hua, Q. Yang, D. Zhang, F. Meng, C. Chen, Z. You, J. Zhang, S. Lv, J. Meng, Microstructures and mechanical properties of a newly developed high-pressure die casting Mg-Zn-RE alloy, J. Mater. Sci. Technol. 53 (2020) 174–184.

[29] S.-Q. Luo, A.-T. Tang, F.-S. Pan, K. Song, W.-Q. Wang, Effect of mole ratio of Y to Zn on phase constituent of Mg-Zn-Zr-Y alloys, Trans. Nonferrous Metals Soc. China 21 (2011) 795–800.
[30] D. Qiu, M.X. Zhang, J.A. Taylor, P.M. Kelly, A new approach to designing a grain refiner for Mg casting alloys and its use in Mg–Y-based alloys, Acta Mater. 57 (2009) 3052–3059.
[31] H.W. Chang, D. Qiu, J.A. Taylor, M.A. Easton, M.X. Zhang, The role of Al2Y in grain refinement in Mg–Al–Y alloy system, J. Magnes. Alloy. 1 (2013) 115–121.
[32] X.H. Shao, Z.Q. Yang, X.L. Ma, Strengthening and toughening mechanisms in Mg–Zn–Y alloy with a long period stacking ordered structure, Acta Mater. 58 (2010) 4760–4771.
[33] G. Bi, Y. Han, J. Jiang, Y. Li, D. Zhang, D. Qiu, M. Easton, Microstructure and mechanical properties of an extruded Mg-Dy-Ni alloy, Mater. Sci. Eng., A 760 (2019) 246–257.
[34] J. Zhang, S. Liu, Z. Leng, X. Liu, Z. Niu, M. Zhang, R. Wu, Structure stability and mechanical properties of high-pressure die-cast Mg–Al–La–Y-based alloy, Mater. Sci. Eng., A 531 (2012) 70–75.
[35] P. Qin, Q. Yang, K. Guan, F. Meng, S. Lv, B. Li, D. Zhang, N. Wang, J. Zhang, J. Meng, Microstructures and mechanical properties of a high pressure die-cast Mg–4Al−4Gd−0.3Mn alloy, Mater. Sci. Eng., A 764 (2019).
[36] W. Wen, A.A. Luo, T. Zhai, Y. Jin, Y.-T. Cheng, I. Hoffmann, Improved bending fatigue and corrosion properties of a Mg–Al–Mn alloy by super vacuum die casting, Scripta Mater. 67 (2012) 879–882.
[37] A.A. Luo, B.R. Powell, M.P. Balogh, Creep and microstructure of magnesium-aluminum-calcium based alloys, Metall. Mater. Trans. A 33 (2002) 567–574.
[38] P. Zhang, Creep behavior of the die-cast Mg–Al alloy AS21, Scripta Mater. 52 (2005) 277–282.
[39] Y. Ali, D. Qiu, B. Jiang, F. Pan, M.-X. Zhang, Current research progress in grain refinement of cast magnesium alloys: a review article, J. Alloys Compd. 619 (2015) 639–651.
[40] Q. Yang, S. Lv, P. Qin, F. Meng, X. Qiu, X. Hua, K. Guan, W. Sun, X. Liu, J. Meng, Interphase boundary segregation induced phase transformation in a high-pressure die casting Mg-Al-La-Ca-Mn alloy, Mater. Des. 190 (2020).
[41] R. Schmid-Fetzer, A. Kozlov, Thermodynamic aspects of grain growth restriction in multicomponent alloy solidification, Acta Mater. 59 (2011) 6133–6144.
[42] Z. Zhang, X. Liu, Z. Wang, Q. Le, W. Hu, L. Bao, J. Cui, Effects of phase composition and content on the microstructures and mechanical properties of high strength Mg–Y–Zn–Zr alloys, Mater. Des. 88 (2015) 915–923.
[43] D. Liu, J. Song, B. Jiang, Y. Zeng, Q. Wang, Z. Jiang, B. Liu, G. Huang, F. Pan, Effect of Al content on microstructure and mechanical properties of as-cast Mg-5Nd alloys, J. Alloys Compd. 737 (2018) 263–270.
[44] J. Jiang, Y. Wang, Y. Li, W. Shan, S. Luo, Microstructure and mechanical properties of the motorcycle cylinder body of AM60B magnesium alloy formed by combining die casting and forging, Mater. Des. 37 (2012) 202–210.
[45] D.H. Kim, J.Y. Lee, H.K. Lim, W.T. Kim, D.H. Kim, Effect of Al addition on the elevated temperature deformation behavior of Mg–Zn–Y alloy, Mater. Sci. Eng., A 487 (2008) 481–487.
[46] Z.H. Huang, S.M. Liang, R.S. Chen, E.H. Han, Solidification pathways and constituent phases of Mg–Zn–Y–Zr alloys, J. Alloys Compd. 468 (2009) 170–178.
[47] C.H. Caceres, G.E. Mann, J.R. Griffiths, Grain size hardening in Mg and Mg-Zn solid solutions, Metall. Mater. Trans. A 42 (2011) 1950–1959.
[48] N. Mo, Q. Tan, M. Bermingham, Y. Huang, H. Dieringa, N. Hort, M.-X. Zhang, Current development of creep-resistant magnesium cast alloys: a review, Mater. Des. 155 (2018) 422–442.
[49] J.A. Yasi, L.G. Hector, D.R. Trinkle, First-principles data for solid-solution strengthening of magnesium: from geometry and chemistry to properties, Acta Mater. 58 (2010) 5704–5713.
[50] N. Tahreen, D.F. Zhang, F.S. Pan, X.Q. Jiang, D.Y. Li, D.L. Chen, Strengthening mechanisms in magnesium alloys containing ternary I, W and LPSO phases, J. Mater. Sci. Technol. 34 (2018) 1110–1118.
[51] J. Zhang, S. Liu, R. Wu, L. Hou, M. Zhang, Recent developments in high-strength Mg-RE-based alloys: focusing on Mg-Gd and Mg-Y systems, J. Magnes. Alloy. 6 (2018) 277–291.
[52] Q. Yang, F. Bu, X. Qiu, Y. Li, W. Li, W. Sun, X. Liu, J. Meng, Strengthening effect of nano-scale precipitates in a die-cast Mg–4Al–5.6Sm–0.3Mn alloy, J. Alloys Compd. 665 (2016) 240–250.
[53] Z. Száraz, Z. Trojanová, M. Cabbibo, E. Evangelista, Strengthening in a WE54 magnesium alloy containing SiC particles, Mater. Sci. Eng., A 462 (2007) 225–229.
[54] C. Zhao, X. Chen, F. Pan, S. Gao, D. Zhao, X. Liu, Effect of Sn content on strain hardening behavior of as-extruded Mg-Sn alloys, Mater. Sci. Eng., A 713 (2018) 244–252.
[55] J.A. Del Valle, F. Carreño, O.A. Ruano, Influence of texture and grain size on work hardening and ductility in magnesium-based alloys processed by ECAP and rolling, Acta Mater. 54 (2006) 4247–4259.
[56] O. Ryen, O. Nijs, E. Sjolander, B. Holmedal, H. Ekstrom, E. Nes, Strengthening mechanisms in solid solution aluminum alloys, Metall. Mater. Trans. A 37 (2006) 1999–2006.
[57] Z. Zhang, J.-H. Zhang, J. Wang, Z.-H. Li, J.-S. Xie, S.-J. Liu, K. Guan, R.-Z. Wu, Toward the development of Mg alloys with simultaneously improved strength and ductility by refining grain size via the deformation process, Int. J. Miner. Metall. Mater. (2020), https://doi.org/10.1007/s12613-020-2190-1.